A comprehensive modeling for the CO2 electroreduction to CO

JPhys Energy

PAPER • OPEN ACCESS

A comprehensive modeling for the CO_2 electroreduction to CO

To cite this article: Matteo Agliuzza *et al* 2024 *J. Phys. Energy* **6** 015004

IOP Publishing J. Phys. Energy 6 (2024) 015004 https://doi.org/10.1088/2515-7655/ad0a39

Journal of Physics: Energy

OPEN ACCESS

RECEIVED
21 August 2023

REVISED
26 October 2023

ACCEPTED FOR PUBLICATION
7 November 2023

PUBLISHED
16 November 2023

PAPER

A comprehensive modeling for the CO_2 electroreduction to CO

Matteo Agliuzza[1,2,*], **Candido Fabrizio Pirri**[1,2] **and Adriano Sacco**[1]

[1] Center for Sustainable Future Technologies @Polito, Istituto Italiano di Tecnologia, Corso Trento 21, 10129 Torino, Italy
[2] Applied Science and Technology Department, Politecnico di Torino, Corso Duca degli Abruzzi 24, 10129 Torino, Italy
[*] Author to whom any correspondence should be addressed.

E-mail: matteo.agliuzza@polito.it

Keywords: CO_2 conversion, carbon monoxide, electrochemistry, model, COMSOL

Supplementary material for this article is available online

Abstract

In the research for the decarbonization processes, electrochemistry is among the most studied routes for the conversion of carbon dioxide in added-value products, thanks to the up-scalability and the mild conditions of work of the technology. In this framework, modeling the electrochemical reactor is a powerful tool to predict and optimize important features of the electroreduction. In this study, we propose a comprehensive modeling for the whole electrochemical reactor, which has been validated through the experiments with good agreement. In particular, the performance of the cell is studied as a function of the voltage applied, for different sizes of the reactor. Furthermore, the model has been used to study the chemical conditions at the cathode surface, as well as electrochemical conditions at different applied biases and flow rates of the electrolyte.

1. Introduction

The global warming is a problem which is becoming increasingly impelling throughout the years. In particular, the human activity is its major cause, due to anthropogenic CO_2 emissions which unbalance the natural lifecycle of carbon [1, 2], leading to increased natural phenomena both in intensity and frequency. In this framework, in order to reduce the carbon accumulation in the atmosphere, the research community has been focusing its attention on the so-called carbon capture and utilization technologies [3]. In particular, electrochemistry is among the most promising routes for the carbon dioxide conversion into fuels through the CO_2 reduction reaction (CO_2RR) approach, thanks to several factors: mild working conditions in terms of pressure and temperature, repeatability of the process, use of non-toxic green reagents as electrolytes, up-scalability [4] and the possibility of the integration with photovoltaics for the sustainability of the device [5–8].

In the field of electrochemical conversion of CO_2 into useful products, many efforts have been made to optimize both the set-up of the reactors and the catalyst. In particular, the design of the reactor influences the electrical parameters of the device (e.g. energy efficiency, current density, *etc*), due to the peculiar characteristics of the different configurations. The catalyst, on the other hand, governs the kinetics of the reactions and the selectivity towards the desired product [9].

Even though the majority of the work in this field is experimental, modeling of the reactors is crucial to consider the influence of key parameters such as local pH [10–12], pressure [13] and temperature [14, 15]. Initially, several mathematical models have been proposed to describe the diffusive boundary layer (DBL) occurring at the cathode's surface. Gupta *et al* [16] modeled the electrode-electrolyte boundary layer to calculate the electrode surface protons and CO_2 concentrations, considering a Cu catalyst in $KHCO_3$ solution. Despite the lack of experimental validation and the limited points of current densities considered, the model showed interesting results on the dependence of the electrode condition on the electrolyte strength and stirring rate. Sacco *et al* [17] analyzed the effect of gas bubbles on the mass transport in the DBL. A good agreement with experimental results has been obtained, and the dependence of the DBL thickness upon the gas bubbles is found. Thanks to COMSOL Multiphysics software, more complicated models of the full

electrochemical cells can be obtained. Wu *et al* [18] presented a model of a microfluidic cell for the reduction of CO_2 in CO, validating the results with experimental data at different flow rates. They showed the dependence of the performance of the full cell on the feed CO_2 rates, length of the channel and porosity of the Gas Diffusion Electrodes involved. Similarly, Kotb *et al* [19] developed the first model of a microfluidic electrochemical cell for the conversion of CO_2 in alcohols (CH_3OH). The simulations reported large discrepancies with respect to the experimental results; nevertheless, they were able to show the dominance of H_2 formation over the CH_3OH production, demonstrating the need of improved CO_2 transport to the cathode for better performance. Singh *et al* [20] modeled a batch electrochemical cell for CO_2 reduction with $KHCO_3$ electrolyte, CO_2 feed and no electrolyte recirculation. The work proposed a thorough study on the parameters which influence the polarization losses of the cell, to minimize the ohmic losses for a more efficient coupling between the photovoltaics and the reactor. However, no experimental validation is reported, and the hydrogen evolution reaction (HER) is not explicitly modeled. Similarly, Luo *et al* [21] simulated a photoelectrochemical reactor for formic acid production in 0.5 M $NaHCO_3$ catholyte and 0.5 M NaOH anolyte; in this case, the photoanode is described by Shockley–Queisser model fitted with the diode relationship, at a light intensity of 100 mW cm^{-2}. The model is validated with experimental data of current density vs. voltage at 1 sun illumination, and the effect of CO_2 flow rate is studied on the current density and efficiency of conversion. Chinnathambi *et al* [22] investigated the mass transport limitations across the electrolyte and the bipolar membrane for formic acid formation at different pressures, up to 40 bar. Also in this case, the model is validated through experimental data of the current density vs. the applied potential. Yang *et al* [23] developed a mathematical model for a two-phase flow for bicarbonate electrolyzer, enhancing the interplay between two-phase flow, ion transport and performance of the device. Obasanjo *et al* [24] also exploited a 1D model (implemented in COMSOL Multiphysics) for a bicarbonate-fed electrochemical reactor for CO_2 conversion in methane (CH_4), in order to design more efficiently the system with increased performance.

Despite the works described so far, there is a lack in the literature of a comprehensive model which introduces both studies regarding the performance of the cell in a wide range of voltages with varying design parameters, and studies on the chemical conditions across the cell (such as pH or chemical species concentrations). For these reasons, in the present work, we propose a 2D isothermal model of a full batch cell for the conversion of CO_2 to CO in 0.1 M $KHCO_3$ employing Ag cathodic catalyst with electrolyte recirculation. The model has been first validated by comparing the simulations results with ad-hoc designed experiments, and then employed to investigate the effect of the different parameters such as flow rates of the CO_2-saturated electrolyte, pressure, voltage drop on the proton exchange membrane (PEM) and variation of the species at the surface of the cathode and in the DBL, in order to build an all-around comprehensive model for the CO_2 reduction reactor.

2. Batch cell model

Since the chemical properties (*e.g.* species concentrations) and electrochemical properties (*e.g.* current density, partial current densities and product selectivity) are assumed to be invariant with respect to the depth of the cell, the experimental batch-cell reactor is modeled through a 2D geometry (depicted in figure 1) in COMSOL Multiphysics 6.1. Cathode and anode electrodes, respectively Ag and Pt nanoparticles, are simulated by infinitely thin films at the boundaries of the simulation domain, and the cathodic/anodic compartments are separated by a Nafion 117 PEM. Both catholyte and anolyte are 0.1 M aqueous $KHCO_3$ solutions, which recirculate through the compartments: the electrolyte is saturated with CO_2 in external reservoirs before entering the inlets, and then exits through the outlets bringing all the products of the electrochemical reactions (CO, H_2 and O_2). In this regard, the products are assumed to be in liquid phase, despite their low solubility at ambient pressure: the assumption is made to avoid unreasonable complexities in the model. Moreover, the system is isothermal, meaning that the temperature T is fixed at 298.15 K: since the electrolyte is diluted, the heating due to the (small) current can be considered negligible.

In the following, some highlights of the mathematical model are provided, regarding the different domains of the simulation.

2.1. Electrolyte domain

The ionic current distribution inside the electrolyte domains has been obtained thanks to the sum of the ionic fluxes of the single ionic species present in the electrolyte:

$$J_e = F\sum_i z_i N_i \tag{1}$$

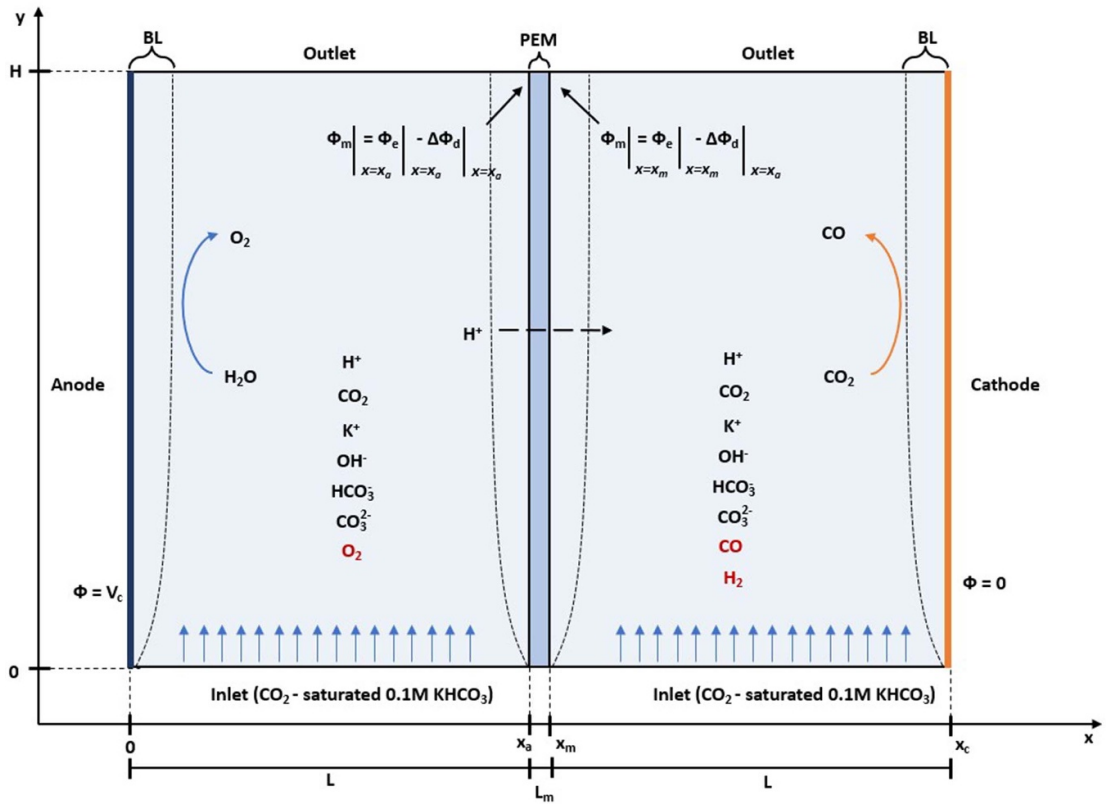

Figure 1. Schematic representation of the cell configuration. Φ_m represents the membrane potential, Φ_e the electrolyte potential and V_c is the voltage applied to the cell. The two compartments have the same length L and height H, while the membrane length is L_m; x_a, x_m, x_c represent the x coordinates of the anodic/membrane/cathodic boundaries respectively.

where J_e is the electrolyte current density, F the Faraday constant, z_i the charge number of the i-th species (where $i = CO_2, K^+, OH^-, H^+, HCO_3^-, CO_3^{2-}, H_2, CO, O_2$) and N_i the ionic mass flux. Please notice that, for neutral species, the charge number is equal to zero, therefore their contribution to the overall current is null. The ionic mass flux be calculated by means of the Nernst–Planck equations, which describe the motion of chemical species in a fluid considering diffusion, electromigration and convection:

$$N_i = \underbrace{-D_i \nabla c_i}_{\text{diffusion}} \underbrace{- z_i u_{\text{mob},i} F c_i \nabla \Phi_e}_{\text{migration}} + \underbrace{c_i u}_{\text{convection}} . \tag{2}$$

In the first diffusion term, D_i is the diffusion coefficient and c_i the species concentration; in the second migration term, $u_{\text{mob},i}$ refers to the species mobility, and Φ_e the electrolyte potential; lastly, in the convection term, u is the electrolyte velocity. The mobility is calculated by means of the Nernst–Einstein relation, which reads as follows:

$$u_{\text{mob},i} = \frac{D_i}{RT} \tag{3}$$

where R is the molar gas constant and T the temperature. Furthermore, in the electrolyte domains, the electroneutrality condition holds, for which:

$$\sum_i z_i c_i = 0. \tag{4}$$

Regarding the species mass continuity, the following equation holds in the electrolyte domain:

$$\nabla \cdot N_i + u \cdot \nabla c_i = R_i \tag{5}$$

where R_i is the mass source term for each species: since this term is related to the consumption/formation of the single species, it is equal to 0 in the electrolyte (where only equilibrium reactions occur) and different

Table 1. Diffusion coefficients (at infinite dilution) and initial equilibrium concentrations for the ionic species, at T = 298.15 K. Since O_2, CO and H_2 are the products of the electrochemical reactions, their initial concentration is set to zero. H^+ concentration is defined such that the bulk pH is set equal to 6.8 [16].

Chemical species	Diffusion coefficient ($m^2\ s^{-1}$)	References	Initial equilibrium concentration (M)	References
CO_2	1.91×10^{-9}	[16]	0.0342	[16]
K^+	1.95×10^{-9}	[26]	0.1	—
OH^-	5.27×10^{-9}	[16]	6.6×10^{-8}	[16]
H^+	9.3×10^{-9}	[27]	1.5×10^{-7}	*Calc.*
HCO_3^-	1.10×10^{-9}	[26]	0.099	[16]
CO_3^{2-}	9.23×10^{-10}	[28]	3.1×10^{-5}	[16]
H_2	4.5×10^{-9}	[29]	0	—
CO	2.03×10^{-9}	[29]	0	—
O_2	2.10×10^{-9}	[29]	0	—

from zero only on the cathode/anode boundaries (see equation (22) below). Finally, the charge conservation is considered:

$$\nabla \cdot J_e = 0. \tag{6}$$

When CO_2 dissolves in water (or in water-based electrolytes), several reactions occur. In the system under study, carbonate/bicarbonate reactions are implemented, along with the self-ionization process of water (equilibrium constants are from Sullivan *et al* [25]):

$$\mathrm{HCO_3^- + OH^- \overset{K_1}{\Leftrightarrow} CO_3^{2-} + H_2O} \quad \left(K_1 = 4.66 \times 10^3\ 1/\mathrm{M}\right) \tag{7}$$

$$\mathrm{CO_2 + OH^- \overset{K_2}{\Leftrightarrow} HCO_3^-} \quad \left(K_2 = 4.44 \times 10^7 \mathrm{M}\right) \tag{8}$$

$$\mathrm{H_2O \overset{K_f}{\Leftrightarrow} H^+ + OH^-} \quad \left(K_f = 10^{-14}\mathrm{M}^2\right). \tag{9}$$

Since the reactions are fast, they are considered as equilibrium reactions in any point of the domain. They are important to balance the concentrations of the species along the cell, especially in the boundary layers where CO_2 (H^+) is consumed at the surface of the cathode (anode).

Lastly, the recirculation is simulated by assigning a value u_0 to the y-component of u (in equation 2), and the x-component set to zero: in this way, it is possible to create a flow from the inlet boundary towards the outlet with velocity u_0. The concentrations of the ionic species introduced in the inlet are taken as the initial concentration values which satisfy the equilibrium reactions: in this way, it is possible to simulate the injection of a CO_2-saturated electrolyte in the domain. The initial concentrations and diffusion coefficients of the species simulated are given in table 1.

2.2. Membrane domain

Nafion 117 membrane is modeled through a porous matrix of fixed negative space charges, with a concentration much higher with respect to the concentration of protons, which is the only positive species allowed to migrate from anode towards the cathode. The chosen parameters for the ion exchange membrane are fixed charge concentration $C_m = 1$ M, and conductivity $\sigma_m = 12\ \mathrm{S\ m^{-1}}$. At the membrane domain boundaries, the potential shift is given by the Donnan potential Φ_d, which can predict the membrane potential when high density of membrane-fixed charges is assumed [30, 31]. In particular, the Donnan potential is related to the concentration of protons at the boundaries of the membrane, such that:

$$\Delta\Phi_d = \frac{RT}{F} \ln\left(\frac{[H^+]}{C_m}\right). \tag{10}$$

The potential on the membrane Φ_m, therefore, can be calculated considering the contribution of the Donnan potential to the value of the electrolyte potential Φ_e on the membrane boundaries (figure 1):

$$\Phi_m\left(x = x_a, x_m\right) = \Phi_e\left(x = x_a, x_m\right) - \Delta\Phi_d\left(x = x_a, x_m\right) \tag{11}$$

where the dependency on x in the Donnan potential lies in the concentration of protons. The membrane current density i_m in this case is expressed by the Ohm's law, which reads:

$$i_m = -\sigma_m \Delta\Phi_m \tag{12}$$

and, finally, the normal molar flux of protons N_{H^+} is related to the normal membrane current density through the Faraday's Law:

$$N_{H^+} = \frac{i_m}{F}. \tag{13}$$

Continuity is guaranteed by imposing the normal current density of the electrolyte equal to the normal membrane current density at the boundary.

Additional simulations have been performed considering an anion exchange membrane (AEM) as separator instead of a PEM one, by changing the charge-carrying species in the membrane domain from H^+ to OH^- ions, keeping the concentration of fixed space charge the same ($C_m = 1$ M).

2.3. Cathode/anode boundaries

The electrochemical reactions occur solely at the catalyst surfaces. The modeled cathodic catalyst is a cluster of Ag nanoparticles, which selectively convert CO_2 in CO (CO_2RR, reaction (14)); moreover, HER (reaction (15)) is a competing reaction, and it is inserted in the model as well. For what concerns the anode, only oxygen evolution reaction (OER, reaction (16)) is present, and it is considered non-limiting in the model. The simulated reactions are reported here below, together with their equilibrium potential (reported with respect to the reversible hydrogen electrode, RHE):

$$CO_2 + 2H^+ + 2e^- \leftrightarrow CO + H_2O \quad (E_0 = -0.1\,\text{V vs. RHE}) \tag{14}$$

$$2H^+ + 2e^- \leftrightarrow H_2 \quad (E_0 = 0\,\text{V vs. RHE}) \tag{15}$$

$$2H_2O \leftrightarrow 4H^+ + 4e^- + O_2 \quad (E_0 = 1.23\,\text{V vs. RHE}). \tag{16}$$

In order to study the selectivity of the reactions toward a specific product, Faradaic efficiency (FE) is used as key parameter. It describes the efficiency of the electric charge to participate to a particular electrochemical reaction, and it is calculated through the partial current density ($j_{par,m}$) related to the specific cathodic product ($m = H_2$, CO):

$$FE_m = \frac{j_{par,m}}{J_{tot}} \times 100 \tag{17}$$

where J_{tot} is the total current density passing through the reactor

$$J_{tot} = \sum_m j_{par,m}. \tag{18}$$

The partial current density $j_{par,m}$ is determined through the Butler–Volmer equations, which are widely used when modeling the kinetics of electrodes activity in electrochemical environment [32–34]:

$$j_{par} = j_0 \left[C_R \exp\left(\frac{\alpha_a F}{RT}\eta\right) - C_{OX} \exp\left(-\frac{\alpha_c F}{RT}\eta\right)\right]. \tag{19}$$

Equation (19) represents the concentration-dependent Butler Volmer expression, which relates the partial current density of the reaction to the overpotential (η) through two kinetic parameters: the exchange current density j_0, namely the partial current density at $\eta = 0$, and the cathodic (anodic) charge transfer coefficients α_c (α_a). C_R and C_{ox} are dimensionless expressions for the reduced and oxidized species: for HER, $C_R = C_{ox} = 1$, while for OER, $C_R = 1$, $C_{ox} = 0$. For the conversion of CO_2 to CO (reaction (14)) the expression used for C_{ox} is

$$C_o = \frac{C^s_{CO_2}}{C^*_{CO_2}} \tag{20}$$

where $C^s_{CO_2}$ is the concentration of CO_2 on the electrode surface, and $C^*_{CO_2}$ the bulk concentration. In this way, it is possible to implement the mass-transport limit of CO_2 from bulk to surface when the consumption of CO_2 is much faster with respect to the diffusion process. The kinetic parameters used are taken from experimental Tafel plots and corrected to fit the experimental results: in tables 2 and 3 are reported the kinetic parameters employed for length $L = 0.6$ cm and $L = 0.25$ cm respectively. Please note that small changes can be noticed in the two cases, meaning that a change in the setup leads to slight changes in the kinetics as well.

The overpotential is expressed by the difference of the applied potential on the electrode (Φ_s) and the equilibrium potential for the reaction to occur ($r = CO_2$RR, HER, OER):

$$\eta_r = \Phi_s - E_{o,r} - \Phi_e. \tag{21}$$

Table 2. Kinetic parameters for the electrochemical reactions, at semi-cell length L = 0.6 cm.

Reaction	j_0 (A m^{-2})	α_c	α_a	C_r	C_{ox}
CO_2RR	7.2×10^{-7}	0.25277	0.74723	1	$C^s_{CO_2}/C^*_{CO_2}$
HER	9.0×10^{-5}	0.14437	0.85563	1	1
OER	10.0	—	1	1	0

Table 3. Kinetic parameters for the electrochemical reactions, at semi-cell length L = 0.25 cm.

Reaction	j_0 (A m^{-2})	α_c	α_a	C_r	C_{ox}
CO_2RR	7.2×10^{-7}	0.23708	0.76292	1	$C^s_{CO_2}/C^*_{CO_2}$
HER	2.6×10^{-5}	0.15399	0.84601	1	1
OER	10.0	—	1	1	0

At last, a mass source term is introduced in the normal species flux on the electrodes surfaces due to the electrochemical reactions:

$$N_i = \frac{\nu_i j_{\text{par}}}{nF} \tag{22}$$

where ν_i are the stoichiometric coefficients of the species involved in the reactions, and n the number of electrons involved (n is equal to 2 for CO and H_2, and equal to 4 for O_2).

2.4. Numerical processing

The previous equations are implemented in COMSOL Multiphysics 6.1. Both electrolyte domains and electrode boundaries are modeled through the tertiary current distribution (TCD) interface [35]; for the membrane domain, since no significant gradients of concentrations are expected, it has been simulated through secondary current distribution interface [36], while the Donnan potentials are retrieved by coupling with the TCD interface. Finite element method is used to solve the partial differential equations, and a user-defined mesh is exploited with rectangle-shaped mesh elements: the mesh is mapped such that it is finer in the membrane/electrode boundaries and coarser in the bulk of the anodic/cathodic compartments. In the end, the mesh contains 782 boundary elements and 19 095 domain elements.

3. Experimental

The experimental setup used to validate the model is depicted in figure 2. The device is composed by a commercial electrochemical reactor (ElectroCell) with ethylene-propylene diene monomer gaskets exploited to create the anodic/cathodic compartments, and a Nafion N117 (from Ion Power) PEM that acts as separator.

The electrolyte (0.1 M of $KHCO_3$ 99.7% purity from Sigma Aldrich in distilled water) is recirculated through external reservoirs thanks to a peristaltic pump (Ismatec MCP ISM404B) at a flow equal to 1.547 ml min^{-1}; the CO_2 is directly bubbled inside the electrochemical cell through two Bronkhorst mass-flows, set at 15 ml min^{-1}.

For what concerns the electrodes, in the anode a commercial Pt foil from GoodFellow (geometric area 9.9 cm^2) is exploited for the oxygen evolution reaction, and for the cathode silver nanoparticles are deposited by physical sputtering technique (current of deposition $I_{\text{dep}} = 50$ mA, time of deposition $T_{\text{dep}} = 300$ s) on a Carbon Paper substrate (28BC from SGL Carbon), following the procedure developed by our group [37] (field-emission scanning electron microscope images are reported in figures S1 and S2 available in the supplementary information): in this case, the cathodic geometric area varies slightly between the experiments, ranging from 1.2 to 1.9 cm^2. A picture of the cathode mounted on the current collector is present in figure S3 of the supplementary information. In both cathodic and anodic compartments, plastic meshes are exploited to break the bubbles that form inside the electrolyte.

Finally, the experiments are performed by chronoamperometries with a BioLogic VSP potentiostat, for which a voltage is applied in a 2-electrode configuration and the current is collected as a function of time (approximately 1 h for each voltage point); the gaseous output of the cathode is sampled by means of a Inficon Fusion Micro Gas Chromatograph, equipped with two modules (a Rt-Molsieve 5 A column and a Rt-Q-Bond column) and a micro thermal conductivity detector for each module. No traces of liquid products were detected in the catholyte through high-performance liquid chromatography (Shimadzu), employing a ReproGel column (300 × 8 mm) and an ultraviolet–visible detector set at 210 nm, with 9.0 mM H_2SO_4 as mobile phase.

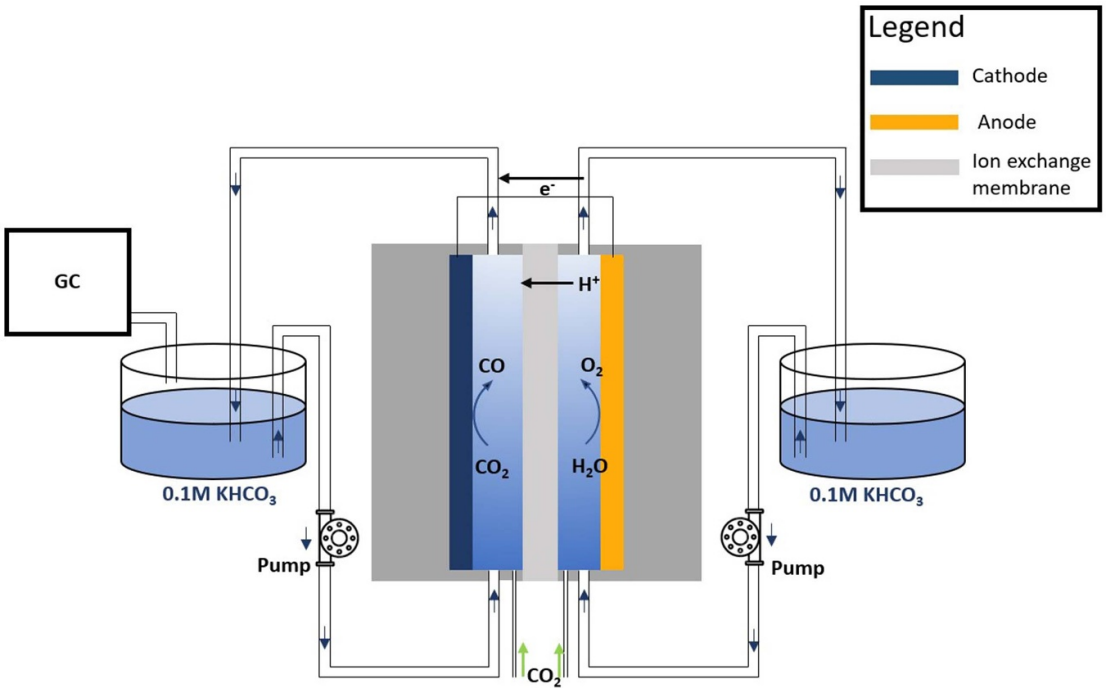

Figure 2. Simplified diagram of the experimental setup. In the cathodic compartment, the electrolyte reservoir is sealed such that the gas inside can be sampled by the gas chromatograph (GC).

The experiments are carried out at least in duplicate, in order to guarantee the reproducibility of the obtained results.

The formula used to retrieve the experimental Faradaic efficiencies is:

$$FE_m = \frac{nFf_{CO_2}\chi}{vi_{tot}} \times 100 \tag{23}$$

where n is the number of electrons involved in the reaction ($n = 2$ in HER and CO_2RR case), f_{CO_2} is the flux of CO_2, χ the quantity of the product of interest, v the volume of an ideal gas at standard temperature and pressure condition ($v = 22.41\ \mathrm{l\ mol^{-1}}$) and i_{tot} is the total current flowing through the reactor.

4. Results and discussion

As reported in section 2 and figure 1, the 2D model retrieves results which depend on x and y coordinates. In this simulation, all the data are collected by averaging the results across the y dimension. In order to investigate the effect of the y coordinate, in figure 3 are reported, as an example, the partial current densities of CO and H_2 across this axis, along with their average values, considering the total height H of the cathode fixed at 2 cm (the value is related to the dimension of the real electrode used in the experimental work). It can be observed that the calculated average values represent well the values along y, except at $y = 0$: in this point, there is the inlet boundary, where the electrolyte enters the domain and instant reactions lead to increase of the current. Similar results were obtained for all the quantities (FEs, potentials, concentrations, etc…) obtained by the model. Overall, the average value can be thus considered reliable to represent each quantity along the y axis. For this reason, in the following, we report and discuss the average values of each quantity.

4.1. Model validation

In order to validate the model, experimental CO_2RR tests have been conducted. Figure 4 shows the trend of current density and FEs (of CO and H_2) as a function of the cell voltage applied, with data retrieved by the experimental results and the simulations, at two different semi-cell lengths $L = 0.6$ cm (figures 4(a) and (c)) and $L = 0.25$ cm (figures 4(b) and (d)). The velocity of the electrolyte used for the two cells are respectively $u_0 = 0.0057\ \mathrm{m\ s^{-1}}$ and $u_0 = 0.0067\ \mathrm{m\ s^{-1}}$, which represent a volumetric mass flow of 15 ml $\mathrm{min^{-1}}$. The bigger velocity in the second case is related to the smaller section area: by fixing the volumetric mass, the inward velocity would be higher with smaller perpendicular section area.

The model fits well the experimental data in the investigated voltage recorded (below $V_c = 3$ V the concentrations of products are low, so that the evaluation of the selectivity may result unreliable; therefore,

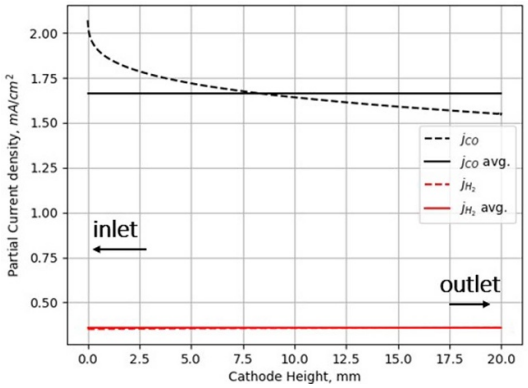

Figure 3. Partial current densities of CO and H_2 as a function of the y coordinate at the cathode surface, for a fixed voltage $V_c = 3$ V. In dashed lines, the current densities as a function of the cathode height are reported; the straight lines report the average values.

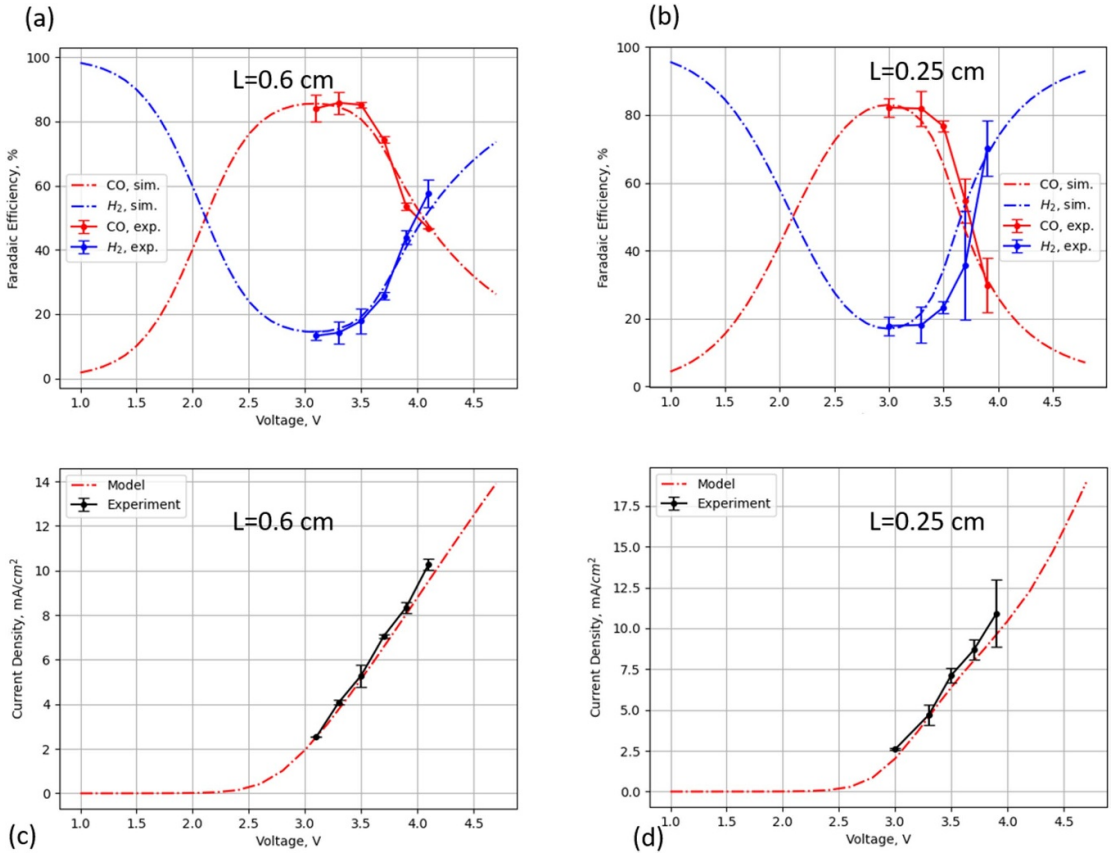

Figure 4. Experimental and model results, showing Faradaic efficiencies and current densities with different semi-cell length. (a), (c) L = 0.6 cm, (b), (d) L = 0.25 cm.

only tests for $V_c \geqslant 3$ V are reported. Moreover, the model can predict the differences present at different lengths L. For example, the current density at $L = 0.25$ cm (figure 4(d)) is higher than the one at $L = 0.6$ cm (figure 4(c)), due to a smaller resistance of the electrolyte and stronger migration of the ionic species. Moreover, the window of selectivity toward CO is well fitted by the simulations: at low voltages (below $V_c \sim 2$ V) hydrogen is predominant due to higher overpotentials of the CO_2RR reaction; at high voltages (over $V_c \sim 4$ V) mass transport limitation of the CO_2 molecules occurs, and so the hydrogen production is relevant. From 2 up to 4 V, thanks to a balance between the rate of the electrochemical reaction and the transport of the CO_2 on the cathode surface, the CO production is efficient. Although the voltage range depends on the experimental setups, the result is widely known and validated in literature [38]. By changing the dimension of the cell, no important changes in the FEs can be noticed.

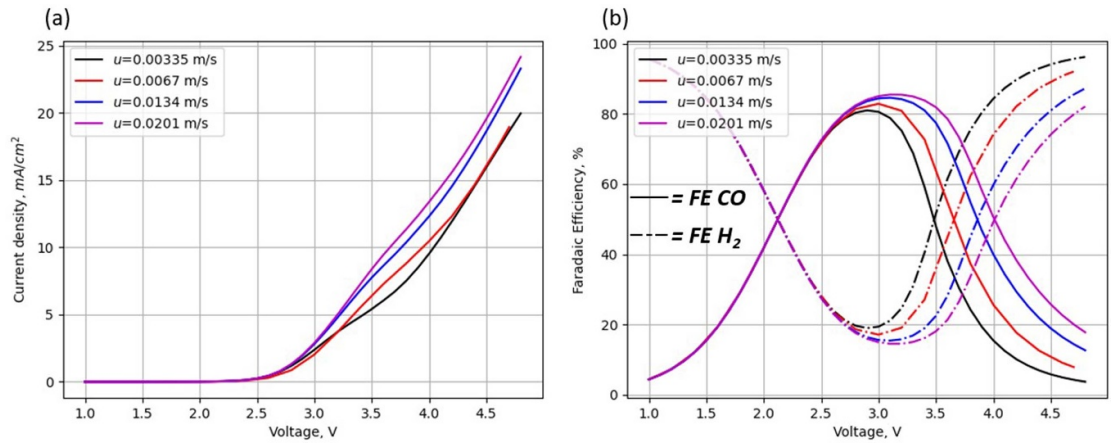

Figure 5. Model results of the (a) current densities and (b) faradaic efficiencies for four different inflow velocities u, as a function of the cell voltage applied. The semi-cell length used is L = 0.25 cm.

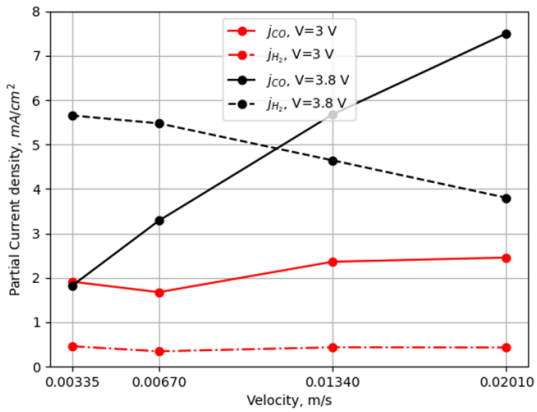

Figure 6. Partial current densities of CO and H_2 production with three different electrolyte inflow velocities, at $V_c = 3$ V (in red) and $V_c = 4$ V (in black).

Based on these outcomes, we considered our model validated through experiments, and in the following we present the results of different simulations.

4.2. Effect of the flow rate

In the model, all the species are assumed to be in liquid phase for simplicity. In this case, the CO_2 feed rate can be increased by increasing the velocity u of the inflow of the electrolyte in the domain: with fixed length $L = 0.25$ cm, the results are depicted in figure 5.

In accordance with Wu *et al* [18], while an increase in the current can be appreciated with higher flow rates (figure 5(a)), the most noticeable result is the increase in the window of selectivity towards CO (figure 5(b)). In particular, the voltage at which FE_{CO} overcomes FE_{H2} is the same (2.2 V), but the mass transport limits become less important due to higher CO_2 feed and, as a result, the CO_2RR is prominent in a wider range of voltages. This phenomenon can also be appreciated by looking at the partial current densities of the electrochemical reactions: in figure 6, j_{CO} and j_{H_2} are plotted as a function of the electrolyte velocity for two fixed voltages applied, $V_c = 3$ V and $V_c = 3.8$ V. The curves show that, at higher voltages, the CO partial current density increases for higher flow rates, while j_{H_2} decreases.

4.3. Study of the boundary layer

In the bulk of the electrolyte no interesting features can be observed: in particular, the concentration of the chemical species is the same as the equilibrium ones entering in the domain through the inlet. The most interesting region is the boundary layer, in which the concentrations differ from the bulk: the electroreduction at the interface, and the contemporary action of the equilibrium reactions, change the concentrations from the initial conditions, leading to predominant diffusion (due to the gradient of concentration) of ionic species in this region. In figure 7 it has been reported some concentration profiles

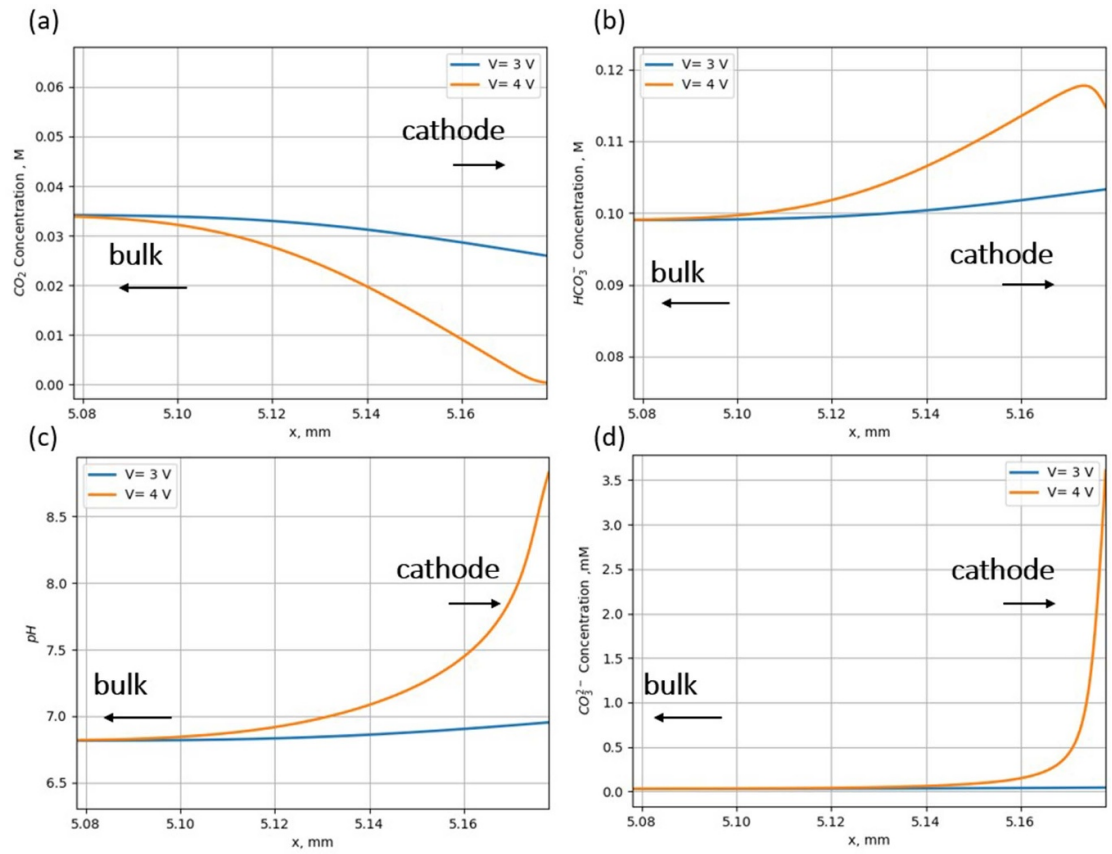

Figure 7. Study of the chemical conditions at the DBL on the cathode's surface, for two different voltages applied: $V_c = 3$ V and $V_c = 4$ V.

along the DBL ($\sim 100\,\mu$m), and the change in pH as well. The data reported are given at fixed flowrate $u_0 = 0.0067$ m s^{-1}.

The chemical conditions going toward the bulk (at $x = 5.08$ mm) is the same as the initial equilibrium one: the pH is 6.8 and the values of the concentrations of the chemical species retrieved are equal to the one used in the inlet (table 1). By moving toward the cathode surface, it can be noticed that the CO_2 concentration starts to reduce (figure 7(a)), due to the consumption at the electrode: the higher the voltage, the higher is the consumption rate. In this framework, due to a re-balance given by the equilibrium chemical reactions (reactions (7)–(9)), it can be observed a change in the concentration of the other species as well, like bicarbonate (figure 7(b)) or carbonate ions (figure 7(d)). An increase in the pH can be noticed as well (figure 7(c)), which increases with the increasing of CO_2 consumption [39]. Similar results has been obtained by Gupta *et al* [16].

The surface CO_2 concentration and surface pH are also reported as a function of the voltage applied (figures 8(a) and (b)), which further prove the decrease of CO_2 concentration, and a subsequent increase in the pH, with the voltage.

4.4. Membrane potential

Lastly, the ohmic losses related to the membrane are investigated (figure 9). Similarly to what have been reported in literature on PEM fuel cell modeling works [40, 41], the membrane shows higher resistance (i.e. higher potential drops) with increasing current density and voltage in the simulation. Moreover, different slopes are visible in the different region of selectivity toward CO or H_2. It is hypothesized that, with increasing concentration of protons inside the membrane pores, capacitive effects occur that screen the electric field and increase the ohmic losses at higher voltages. Further studies are required in this framework to verify the assumptions.

4.5. Effect of anion exchange membrane

It is worth noting that a lot of effort has been done in the scientific community to implement AEMs in the electrochemical reactors for CO_2 reduction: in particular, the OH^- transport from cathode to anode allows for more alkaline conditions which are favorable for CO_2RR, by lowering the concentration of protons thus

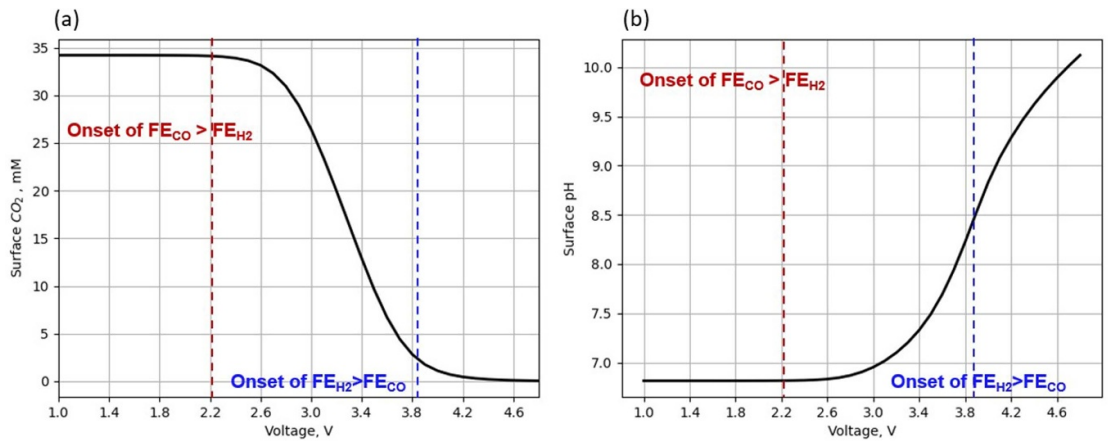

Figure 8. CO_2 concentration (a) and pH change (b) at the cathode's surface, as a function of the voltage applied. Dashed red and blue lines depict the onsets after which the reactor is more selective toward CO and H_2 production, respectively.

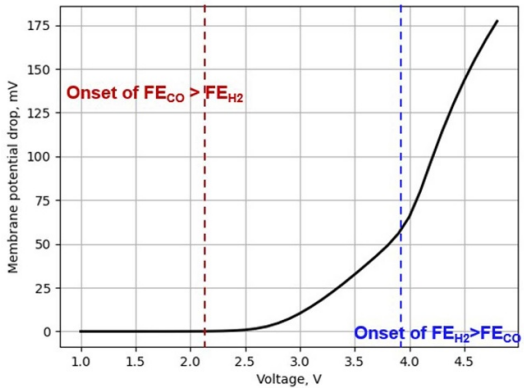

Figure 9. Potential drop across the ion-exchange membrane as a function of the voltage applied.

inhibiting the unwanted HER reaction [42]. In the simulation carried out employing AEM instead of PEM, no appreciable differences have been noticed, and both the current density and faradaic efficiencies are the same. In fact, despite few works report experiments conducted in batch cell with AEM implemented [43–45], there is no study on the difference in performance between AEM and CEM in batch cell environment: the reason is that, since the electrodes are distant from the membrane and the diffusion coefficients of protons and hydroxyl ions are comparable, no difference is present on the chemical conditions on the catalyst surface. For these reasons, the AEM is mostly exploited in zero-gap cells where the cathode and anode are pressed on the membrane, with respect to batch cell configuration.

5. Conclusions

A comprehensive COMSOL model of a reactor for CO_2 reduction is presented, which considers the catalyst kinetics, electrochemical/equilibrium reactions, diffusion/migration and convection of the chemical species, and recirculation of the electrolyte inside the compartments. The model successfully replicates the experimental data of both current density and products faradaic efficiencies (CO and H_2) as a function of the voltage applied, and it is useful to study in deep different phenomena occurring inside the reactor. First of all, the chemical conditions in space can be investigated, such as the variation of the chemical species concentrations in the DBL. The model retrieved the influence of the voltage applied on the CO_2 consumption, with a subsequent increase in the local pH on the cathode surface (from 6.8 up to 10.3). Secondly, the model predicts the performance of the device varying different parameters, such as the inflow velocity and the electric bias applied. In particular, an increase in the current as a function of the inflow velocity is appreciated, as well as bigger window of selectivity towards CO due to higher CO_2 feed rates. Lastly, the simulation can be used as a powerful technique to study the performance when scaling up (or down) the reactor, in view of a future industrial implementation of CO_2RR technologies.

Future improvements in the model are currently under investigation, including the integration of solar cells as power suppliers, by defining the laws which relate the photocurrent with respect to the intensity of the illumination; moreover, the implementation of gas diffusion electrodes will allow to simulate flow cell reactors. Lastly, different catalysts can be simulated, in conditions different from the ambient ones. These topics will be discussed in a forthcoming paper.

Author contributions

Matteo Agliuzza: Writing—review & editing, Writing—original draft, Investigation, Methodology, Data curation, Validation, Conceptualization. **Fabrizio Candido Pirri:** Project administration, Resources, Writing- review & editing. **Adriano Sacco:** Conceptualization, Data curation, Methodology, Supervision, Writing- review & editing.

Data availability statements

The data cannot be made publicly available upon publication because no suitable repository exists for hosting data in this field of study. The data that support the findings of this study are available upon reasonable request from the authors.

Acknowledgments

The author Matteo Agliuzza would like to thank the Italian Ministry of Education (MIUR) for the Ph.D. fellowship funded under the National Research and Innovation Operational Program 2014–2020 (CCI 2014IT16M2OP005), ESF REACT-EU resources, Action IV.4 'Doctorates and research contracts on innovation topics' and Action IV.5 'Doctorates on Green topics'.

ORCID iDs

Matteo Agliuzza https://orcid.org/0000-0001-8937-4292
Candido Fabrizio Pirri https://orcid.org/0000-0003-4991-9459
Adriano Sacco https://orcid.org/0000-0002-9229-2113

References

[1] Al-Ghussain L 2019 Global warming: review on driving forces and mitigation *Environ. Prog. Sustain. Energy* **38** 13–21
[2] Feely R A, Sabine C L, Lee K, Berelson W, Kleypas J, Fabry V J and Millero F J 2004 Impact of anthropogenic CO_2 on the $CaCO_3$ system in the Oceans *Science* **305** 362–6
[3] Gabrielli P, Gazzani M and Mazzotti M 2020 The role of carbon capture and utilization, carbon capture and storage, and biomass to enable a net-zero-CO_2 emissions chemical industry *Ind. Eng. Chem. Res.* **59** 7033–45
[4] Nattestad A, Wagner K and Wallace G G 2023 Scale up of reactors for carbon dioxide reduction *Front. Chem. Sci. Eng.* **17** 116–22
[5] Agliuzza M, Mezza A and Sacco A 2023 Solar-driven integrated carbon capture and utilization: coupling CO_2 electroreduction toward CO with capture or photovoltaic systems *Appl. Energy* **334** 120649
[6] Kim J, Jeong S, Beak M, Park J and Kwon K 2022 Performance of photovoltaic-driven electrochemical cell systems for CO_2 reduction *Chem. Eng. J.* **428** 130259
[7] Creissen C E and Fontecave M 2021 Solar-driven electrochemical CO_2 reduction with heterogeneous catalysts *Adv. Energy Mater.* **11** 2002652
[8] Sultan S, Hyun Kim J, Kim S, Kwon Y and Sung Lee J 2021 Innovative strategies toward challenges in PV-powered electrochemical CO_2 reduction *J. Energy Chem.* **60** 410–6
[9] Su J *et al* 2022 Recent development of nanomaterials for carbon dioxide electroreduction *SmartMat* **3** 35–53
[10] Zhang Z, Melo L, Jansonius R P, Habibzadeh F, Grant E R and Berlinguette C P 2020 pH matters when reducing CO_2 in an electrochemical flow cell *ACS Energy Lett.* **5** 3101–7
[11] Varela A S 2020 The importance of pH in controlling the selectivity of the electrochemical CO_2 reduction *Curr. Opin. Green Sustain. Chem.* **26** 100371
[12] Schouten K J P, Pérez Gallent E and Koper M T M 2014 The influence of pH on the reduction of CO and CO_2 to hydrocarbons on copper electrodes *J. Electroanal. Chem.* **716** 53–57
[13] Todoroki M, Hara K, Kudo A and Sakata T 1995 Electrochemical reduction of high pressure CO_2 at Pb, Hg and In electrodes in an aqueous $KHCO_3$ solution *J. Electroanal. Chem.* **394** 199–203
[14] Vos R E and Koper M T M 2022 The effect of temperature on the cation-promoted electrochemical CO_2 reduction on gold *ChemElectroChem* **9** e202200239
[15] Lobaccaro P, Singh M R, Clark E L, Kwon Y, Bell A T and Ager J W 2016 Effects of temperature and gas–liquid mass transfer on the operation of small electrochemical cells for the quantitative evaluation of CO_2 reduction electrocatalysts *Phys. Chem. Chem. Phys.* **18** 26777–85
[16] Gupta N, Gattrell M and MacDougall B 2006 Calculation for the cathode surface concentrations in the electrochemical reduction of CO_2 in $KHCO_3$ solutions *J. Appl. Electrochem.* **36** 161–72
[17] Sacco A, Zeng J, Bejtka K and Chiodoni A 2019 Modeling of gas bubble-induced mass transport in the electrochemical reduction of carbon dioxide on nanostructured electrodes *J. Catal.* **372** 39–48

[18] Wu K, Birgersson E, Kim B, Kenis P J A and Karimi I A 2015 Modeling and experimental validation of electrochemical reduction of CO_2 to CO in a microfluidic cell *J. Electrochem. Soc.* **162** F23
[19] Kotb Y, Fateen S-E K, Albo J and Ismail I 2017 Modeling of a microfluidic electrochemical cell for the electro-reduction of CO_2 to CH_3OH *J. Electrochem. Soc.* **164** E391
[20] Singh M R, Clark E L and Bell A T 2015 Effects of electrolyte, catalyst, and membrane composition and operating conditions on the performance of solar-driven electrochemical reduction of carbon dioxide *Phys. Chem. Chem. Phys.* **17** 18924–36
[21] Luo X, Xuan J, Fernandez E S and Maroto-Valer M M 2019 Modeling and simulation for photoelectrochemical CO_2 utilization *Energy Proc.* **158** 809–15
[22] Chinnathambi S, Ramdin M and Vlugt T J H 2022 Mass transport limitations in electrochemical conversion of CO_2 to formic acid at high pressure *Electrochem* **3** 549–69
[23] Yang W, Sun L, Bao J, Mo Z, Du M, Li J and Zhang J 2023 Two-phase flow model to define the mass transport in a bicarbonate electrolyzer for a CO_2 reduction reaction *Ind. Eng. Chem. Res.* **62** 16469–80
[24] Obasanjo C A, Gao G, Crane J, Golovanova V, García de Arquer F P and Dinh C-T 2023 High-rate and selective conversion of CO_2 from aqueous solutions to hydrocarbons *Nat. Commun.* **14** 3176
[25] Sullivan B P, Krist K and Guard H E (eds) 1993 *Electrochemical and Electrocatalytic Reactions of Carbon Dioxide* (Elsevier) (https://doi.org/10.1016/C2009-0-13056-8)
[26] Newman J and Balsara N P 2021 *Electrochemical Systems* (Wiley) (available at: http://scholar.google.com/scholar_lookup?hl=en&publication_year=2004&author=J.+Newman&author=K.+E.+Thomas-Alyea&title=Electrochemical+Systems)
[27] Agmon N 1995 The Grotthuss mechanism *Chem. Phys. Lett.* **244** 456–62
[28] Le Gouellec Y A and Elimelech M 2002 Control of calcium sulfate (gypsum) scale in nanofiltration of saline agricultural drainage water *Environ. Eng. Sci.* **19** 387–97
[29] Cussler E L 2009 *Diffusion: Mass Transfer in Fluid Systems* (Cambridge university press)
[30] Ohshima H and Kondo T 1990 Relationship among the surface potential, Donnan potential and charge density of ion-penetrable membranes *Biophys. Chem.* **38** 117–22
[31] Ohshima H and Kondo T 1988 Membrane potential and Donnan potential *Biophys. Chem.* **29** 277–81
[32] Dickinson E J F and Wain A J 2020 The Butler-Volmer equation in electrochemical theory: origins, value, and practical application *J. Electroanal. Chem.* **872** 114145
[33] Dreyer W, Guhlke C and Müller R 2016 A new perspective on the electron transfer: recovering the Butler–Volmer equation in non-equilibrium thermodynamics *Phys. Chem. Chem. Phys.* **18** 24966–83
[34] Mann R F, Amphlett J C, Peppley B A and Thurgood C P 2006 Application of Butler–Volmer equations in the modelling of activation polarization for PEM fuel cells *J. Power Sources* **161** 775–81
[35] Dickinson E J F, Ekström H and Fontes E 2014 COMSOL Multiphysics®: finite element software for electrochemical analysis. A mini-review *Electrochem. Commun.* **40** 71–74
[36] Ibl N 1983 Current Distribution *Comprehensive Treatise of Electrochemistry: Electrodics: Transport* ed E Yeager, J O M Bockris, B E Conway and S Sarangapani (Springer) pp 239–315
[37] Monti N B D, Fontana M, Sacco A, Chiodoni A, Lamberti A, Pirri C F and Zeng J 2022 Facile fabrication of Ag electrodes for CO_2-to-CO conversion with near-unity selectivity and high mass activity *ACS Appl. Energy Mater.* **5** 14779–88
[38] Hatsukade T, Kuhl K P, Cave E R, Abram D N and Jaramillo T F 2014 Insights into the electrocatalytic reduction of CO_2 on metallic silver surfaces *Phys. Chem. Chem. Phys.* **16** 13814–9
[39] Zhou X, Liu H, Xia B Y, Ostrikov K, Zheng Y and Qiao S-Z 2022 Customizing the microenvironment of CO_2 electrocatalysis via three-phase interface engineering *SmartMat* **3** 111–29
[40] Springer T E, Zawodzinski T A and Gottesfeld S 1991 Polymer electrolyte fuel cell model *J. Electrochem. Soc.* **138** 2334
[41] Rakhshanpouri S and Rowshanzamir S 2013 Water transport through a PEM (proton exchange membrane) fuel cell in a seven-layer model *Energy* **50** 220–31
[42] Habibzadeh F, Mardle P, Zhao N, Riley H D, Salvatore D A, Berlinguette C P, Holdcroft S and Shi Z 2023 Ion exchange membranes in electrochemical CO_2 reduction processes *Electrochem. Energy Rev.* **6** 26
[43] Tang J-K *et al* 2020 Anion exchange-induced single-molecule dispersion of cobalt porphyrins in a cationic porous organic polymer for enhanced electrochemical CO_2 reduction via secondary-coordination sphere interactions *J. Mater. Chem.* A **8** 18677–86
[44] He M, Li C, Zhang H, Chang X, Chen J G, Goddard W A, Cheng M-J, Xu B and Lu Q 2020 Oxygen induced promotion of electrochemical reduction of CO_2 via co-electrolysis *Nat. Commun.* **11** 3844
[45] Wang Y, Niu C, Zhu Y, He D and Huang W 2020 Tunable Syngas formation from electrochemical CO_2 reduction on copper nanowire arrays *ACS Appl. Energy Mater.* **3** 9841–7